Chinese Chemical Letters 37 (2026) 111531

Contents lists available at ScienceDirect

Chinese Chemical Letters

journal homepage: www.elsevier.com/locate/cclet

Physically and chemically crosslinked rare-earth-doped hydrogels with dual fluorescence/conductive sensing abilities

Kunda Yao[a], Yue Shen[a], Chao Chen[b], Fengxiang Qin[a], Shuyan Song[b], Xiaochen Dong[c], Wei Liu[a,b,*]

[a] School of Materials Science and Engineering, Nanjing University of Science and Technology, Nanjing 210094, China
[b] State Key Laboratory of Rare Earth Utilization, Changchun Institute of Applied Chemistry, Chinese Academy of Sciences, Changchun 130022, China
[c] School of Chemistry & Materials Science, Jiangsu Normal University, Xuzhou 221116, China; Key Laboratory of Flexible Electronics (KLOFE) and Institute of Advanced Materials (IAM), Nanjing Tech University, Nanjing 211816, China

ARTICLE INFO

Article history:
Received 7 May 2025
Revised 26 June 2025
Accepted 2 July 2025
Available online 3 July 2025

Keywords:
Hydrogel
Multifunctional
Fluorescence
Rare earth
Dual channel sensor

ABSTRACT

Rare-earth-doped fluorescent hydrogels, while effective for optical sensing, often have limited functionality due to weak physical crosslinking. Stretchable chemically crosslinked conductive hydrogel sensors, essential for adhering to the human body to monitor movements, typically hinder fluorescence. This is caused by the opacity of conductive components, and adhesion molecules like catechol may quench fluorescence. These constraints limit the multifunctional applications of hydrogels that combine both physical and chemical crosslinking. In this study, we blend and polymerize acrylamide (AM), 2-acrylamido-2-methylpropanesulfonic acid (AMPS), and iminodiacetic acid (IDA)-modified carboxymethyl cellulose sodium (CMC–Na) to form hydrogels, while introducing rare-earth elements to achieve synergistic benefits. This novel approach yields hydrogels with low hysteresis, high strain (1150%), ultra-fast response capability (50 ms), and high sensitivity (GF = 5.03), facilitated by the physical crosslinking of rare-earth ions. By adjusting the IDA content or the Eu^{3+}/Tb^{3+} ratio, we can precisely control the hydrogel's brightness, achieving tunable red/yellow/green fluorescence variations through radiative transitions. Additionally, we have developed, for the first time, a fluorescence/conductivity dual-channel sensor that responds to pressure changes by displaying color shifts. This represents a new strategy for multifunctional rare-earth-doped hydrogels and flexible sensing applications.

© 2026 Published by Elsevier B.V. on behalf of Chinese Chemical Society and Institute of Materia Medica, Chinese Academy of Medical Sciences.

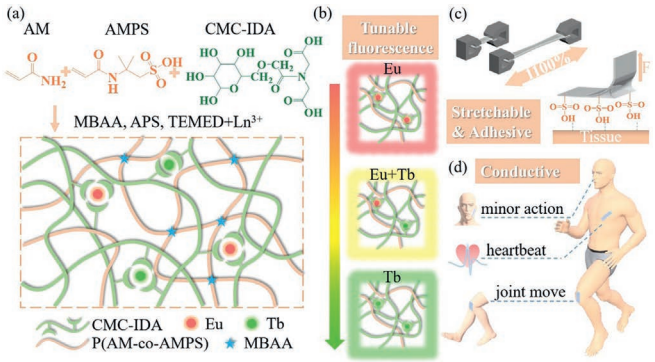
Rare-earth-doped fluorescent hydrogels, an emerging class within the hydrogel family, have attracted significant attention [1–3]. This interest stems from their ability to intelligently sense and respond to external stimuli such as solvents, ions, light, molecules, and mechanical forces [4–7]. The fluorescent response imbues these materials with a form of intelligence, manifested through light signals accompanied by noticeable changes in luminescence, including variations in brightness or color [8–11]. These materials not only imitate natural color-changing systems but also have broad applications in sensors, actuators, biomimetic displays, information encryption, and more [3,12–17]. However, as the range of hydrogels applications continues to expand, single-mode optical displays are no longer sufficient to meet the demands of human-machine interaction, prompting the need for enhanced multifunctionality in these materials [18,19].

Traditional rare-earth-doped fluorescent hydrogels are typically synthesized by grafting small molecule ligands onto the polymer backbone, self-assembling with rare-earth ions through coordination, or employing polysaccharides to achieve the antenna effect [1,20–23]. For instance, the dynamic coordination between rare-earth ions and ligands, such as iminodiacetic acid (IDA) [1,5] and 2,6-pyridinedicarboxylic acid [24], has been used to regulate the fluorochromic response and sol-gel transition of polymer hydrogels in response to various stimuli. Although hydrogels prepared in this way generally exhibit good fluorescence performance and stimulus responsiveness, the weak physical interactions between rare-earth ions and ligands make them prone to breakage under significant external forces, limiting their potential for multifunctional sensing applications [20,22].

In contrast, chemically crosslinked multifunctional hydrogels, due to their robust covalent bonding, typically form stable and tough network structure that can withstand substantial deformation and recover [25–31]. These characteristics have led to their widespread application in strain-resistive sensors for human health

* Corresponding author.
E-mail address: weiliu@ciac.ac.cn (W. Liu).

https://doi.org/10.1016/j.cclet.2025.111531
1001-8417/© 2026 Published by Elsevier B.V. on behalf of Chinese Chemical Society and Institute of Materia Medica, Chinese Academy of Medical Sciences.



Scheme 1. Design strategy for the multi-functional rare-earth-doped hydrogel. (a) Preparation process and chemical architecture *via* free radical polymerization and crosslinking. (b) Fluorescence color variation by tuning rare-earth ions. (c) Stretchability and adhesiveness. (d) Monitoring of body movements.

monitoring. Typically, electrical signal transmission in these hydrogels is achieved by doping with highly conductive materials such as metal nanoparticles [25], grapheme [26], and carbon nanotubes [27], while robust adhesiveness, crucial for stable and precise skin-surface monitoring, is achieved by incorporating catechol-containing components like tannic acid or dopamine [32,33]. However, the addition of these conductive materials often compromises the hydrogel's original transparency, flexibility, or biocompatibility. Moreover, dark conductive media have a detrimental effect on the photoluminescence properties of the hydrogels, particularly by reducing transparency. Additionally, when catechol coexists with rare-earth ions and ligands, the rare-earth ions tend to coordinate with catechol, which acts as an energy acceptor, absorbing energy from the ions through non-radiative transfer rather than releasing it as fluorescence, ultimately causing fluorescence quenching [34,35]. These conflicting interactions make it difficult to fabricate high-performance multifunctional rare-earth-doped hydrogels with both physical and chemical crosslinking. To the best of our knowledge, no rare-earth-doped hydrogel currently exists that successfully integrates fluorescence, conductivity, mechanical properties, and other functionalities.

To address this challenge, we present a novel rare-earth-doped hydrogel featuring both physical and chemical crosslinks, which demonstrates tunable fluorescence, excellent conductive, and superior mechanical and adhesive properties. Our approach involves coupling CMC–Na with IDA through an EDC/NHS condensation reaction. This conjugate (CMC-IDA) is then mixed with AM and AMPS monomers to create a double-network hydrogel *via* free radical polymerization. Eu^{3+} and Tb^{3+} ions are incorporated to establish physical crosslinks with CMC-IDA (Scheme 1a). The rare-earth ions and CMC-IDA function as fluorescence centers and ligands, respectively, enabling modification of the fluorescence color and intensity by varying the Eu/Tb content, IDA concentration, or external factors such as acid, alkali, or metal ions (Scheme 1b). This physical cross-linking also enhances the hydrogel's strength and toughness (Scheme 1c). The chemical crosslinking formed by AMPS and AM establishes the primary network, providing high transparency that facilitates ultraviolet light absorption and fluorescence emission. AMPS, acting as a strong acid electrolyte and adhesive group, imparts excellent conductivity and adhesion properties to the hydrogel, allowing it to detect subtle human movements and function as a dual-channel photoelectric sensor (Scheme 1d).

In a typical procedure, certain amount of CMC was added to a 0.1 mol/L MES solution and stirred at room temperature until fully dissolved. Subsequently, EDC and NHS were then introduced at a molar ratio of $n_{CMC}:n_{EDC}:n_{NHS} = 1:1:1$ and stirred for 30 min to activate the carboxyl groups. An IDA solution, adjusted to pH 5.5 using 0.1 mol/L NaOH, was added to the activated CMC solution to carry out the condensation reaction for 24 h. The solution was dialyzed in a dialysis bag (retaining molecular weight: 3000 Da) against deionized water for 3 days and subsequently lyophilized. After that, the CMC-IDA*x*, AM, and AMPS were thoroughly mixed in deionized water with redox initiators and stirred for 10 min. Finally, the mixture was poured into PTFE molds covered with glass and polymerized at 50 °C for 4.5 h to obtain the hydrogel. The obtained hydrogel were then soaked in 0.1 mol/L rare earth ion solution. The detailed concentration of each reagent are presented in Supporting information.

Fig. 1a illustrates the structural characterization of various CMC-IDA*x* conjugates through FTIR spectra recorded over the 500–4000 cm^{-1} wavenumber range. We observed that in the unmodified CMC sample, a distinct band at 1640 cm^{-1} is absent, while a shoulder appears in the CMC-IDA spectrum. This shoulder is attributed primarily to the C=O stretching vibration of amide I, which forms during the EDC/NHS-mediated amination reaction between the CMC carboxyl (-COOH) groups and the secondary amine (-NH-) of IDA. Additionally, the presence of residual carboxyl groups in IDA may contribute to slight spectral broadening in this region due to hydrogen bonding [36,37]. This feature supports the successful grafting of IDA onto CMC. In the unmodified CMC spectrum, the peak at 3300 cm^{-1} is assigned to the O–H stretching vibrations of hydroxyl (-OH) groups on the CMC backbone, a peak near 2880 cm^{-1} is assigned to the symmetric stretching of CH_2, while a weak peak around 2950 cm^{-1} is attributed to the asymmetric stretching of CH_3 [38–40]. Moreover, the appearance and increased intensity of a peak near 2920 cm^{-1} in the CMC-IDA spectrum suggest a higher degree of IDA incorporation, as additional CH_2 groups from IDA enhance this signal [36,41]. In the carboxylate region, peaks at 1585 and 1411 cm^{-1} correspond to the asymmetric and symmetric stretching vibrations of carboxylate, respectively [42]. The neutralization of IDA with NaOH prior to the condensation reaction enhances the absorption intensities of both peaks in the conjugate, further supporting successful grafting (Fig. 1b and Table S2 in Supporting information). Besides, the amide I band peak at 1647 cm^{-1} (Fig. S1a in Supporting information) confirm the gelatin of the hydrogel, the gradual blue shift of the Vas peaks (Fig. S1b in Supporting information) and the enhanced modulus (Fig. S2 in Supporting information) suggest the formation of CMC-IDA/RE^{3+} complexes.

Fig. 1c and Fig. S3 (Supporting information) present SEM images of the freeze-dried hydrogels, illustrating a notable decrease in pore morphology following rare-earth doping and IDA grafting, which indicates enhanced crosslinking intensity from rare-earth elements. We further explored the fluorescence properties of the rare-earth-doped hydrogels. According to Crosby and Whan's theory, electrons are excited to a vibrational level of the first excited single state ($S_0 \rightarrow S_1$), with energy transfer occurring from the singlet state (S_1) to the triplet state (T_1) through intersystem crossing (ISC) [43–45]. The energy from T_1 is then non-radiatively transferred to Eu and Tb ions, moving from the $^5D_0$ level to the ^7F levels and from the $^5D_4$ level to the ^7F levels, resulting in red and green emissions (Fig. 1d). The fluorescence spectra indicate that intensity increases with IDA concentration, regardless of whether one or two types of rare-earth elements are doped (Fig. 1e and Fig. S4 in Supporting information). This suggests that IDA introduces more coordination sites for RE^{3+}, enhancing the formation of CMC-IDA/RE^{3+} complexes that sensitize the rare-earths. Emission peaks for all Tb^{3+} and Eu^{3+}+Tb^{3+} doped hydrogels at 486, 541, 585, and 621 nm correspond to the $^5D_4 \rightarrow {}^7F_6$, $^5D_4 \rightarrow {}^7F_5$, $^5D_4 \rightarrow {}^7F_4$, and $^5D_4 \rightarrow {}^7F_3$ transitions, respectively. In contrast, the Eu^{3+} doped hydrogels show only two peaks at 592 and 615 nm, correlating with the $^5D_0 \rightarrow {}^7F_1$ and $^5D_0 \rightarrow {}^7F_2$ transitions. As depicted in Fig. 1f, the fluorescence color of the hydrogel can be tuned by adjusting the Eu^{3+}/Tb^{3+} molar ratio, exhibiting strong Tb^{3+} emission at lower

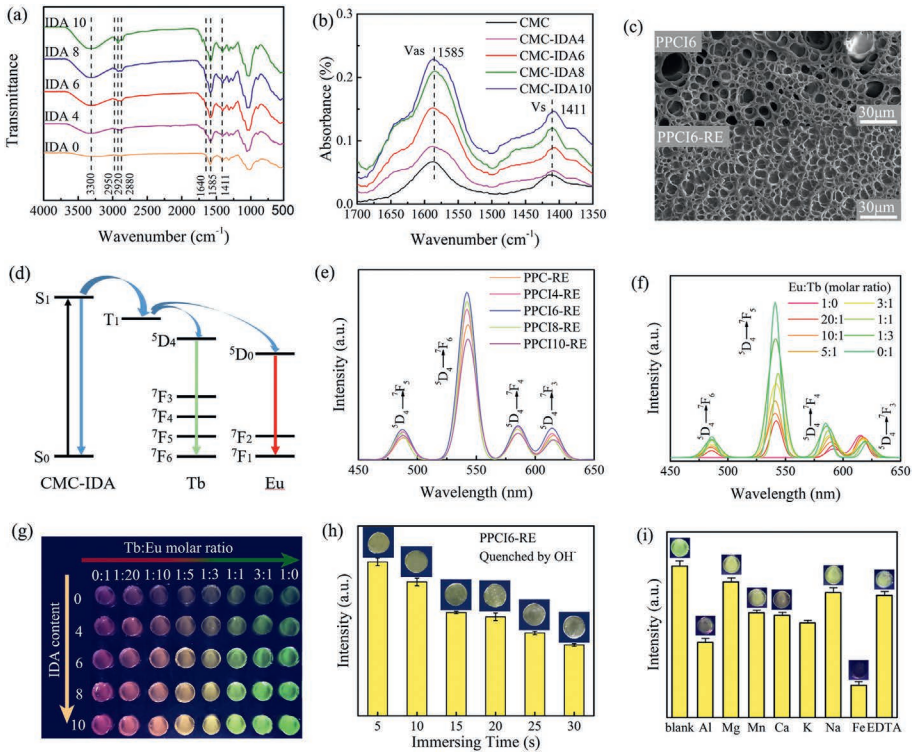


Fig. 1. (a) FTIR spectra of CMC-IDA*x*. (b) Absorption peaks for COONa asymmetric and symmetric stretching vibrations. (c) SEM images of lyophilized PPCI6 and PPCI6-RE hydrogels. (d) Energy transfer processes in rare-earth complexes. (e) Fluorescence spectra of PPCI*x*-RE hydrogels. (f) Fluorescence spectra of PPCI6-RE hydrogel with varying Eu/Tb ratios. (g) Fluorescence color change of PPCI6-RE hydrogel with IDA content or Tb/Eu ratio. (h) Fluorescence quenching of PPCI6-RE hydrogel in 0.1 mol/L NaOH. (i) Fluorescence quenching in different 0.1 mol/L ionic solutions.

ratios and dominant Eu^{3+} emission at higher ratios. Photographs of hydrogels with varying Eu^{3+}/Tb^{3+} ratios and IDA contents (Fig. 1g) reveal significant fluorescence color changes, confirming the spectral results. Additionally, the high transparency of our hydrogel enhances fluorescence emission (Fig. S5 in Supporting information). To assess the responsiveness of the hydrogel's fluorescence to external stimuli, we first immersed the rare-earth-doped hydrogels in a 0.1 mol/L NaOH solution, resulting in a rapid decrease in fluorescence intensity. This indicates the dissociation of CMC-IDA/RE^{3+} coordination bonds under alkaline conditions (Fig. 1h). Remarkably, the fluorescence intensity largely returned after re-immersing in 0.1 mol/L HCl, suggesting potential applications for ionic encryption/decryption (Fig. S6). To test fluorescence responsiveness to metal ion stimuli, we immersed the hydrogel in seven typical metal ionic solutions (0.1 mol/L K^+, Ca^{2+}, Na^+, Mg^{2+}, Mn^{2+}, Al^{3+}, and Fe^{3+}) for 2 min (Fig. 1i). The fluorescence exhibited varying degrees of quenching, with the most significant reductions observed in Fe^{3+} and Al^{3+} solutions, likely due to their ability to accept electrons from ligands, thereby weakening the "antenna effect". Following immersion in EDTA, the fluorescence of the Fe^{3+}-soaked hydrogel recovered, attributed to the stability of the Fe^{3+}-EDTA complex, which prevents Fe^{3+} from occupying CMC-IDA coordination sites. XPS O 1s spectra also reveals the coordination of CMC-IDA/RE^{3+} as well as the quenching by Fe^{3+} and NaOH (Fig. S7 in Supporting information). Given that Fe^{3+} ions can effectively quench the hydrogel's fluorescence, we used an Fe^{3+} solution to inscribe an invisible messages ("FE") on the hydrogel surface. Under daylight, the original and Fe^{3+}-treated hydrogels appear identical (Figs. S8a and b in Supporting information); however, under UV light, the fluorescence of the treated region is quenched, clearly revealing the hidden message (Figs. S8c and d in Supporting information). This demonstration highlights the potential of the fluorescence response in information encryption. Additionally, our hydrogel exhibits an excellent resistance to high humidity and UV exposure, which maintains fluorescence intensity after experiencing 100 %–60 % humidity for 48 h or UV exposure for 96 h (Figs. S9 and S10 in Supporting information).

The mechanical and conductive properties of the as-prepared PPCI*x* and PPCI*x*-RE hydrogels were investigated. All five hydrogel compositions exhibited significant improvements in strength and toughness following rare-earth doping and crosslinking (Fig. 2a). The rare-earth-doped hydrogels showed that fracture strength and elongation initially increased with higher IDA content, reaching peak values in PPCI6-RE at 216 kPa and 1150 %, representing improvements of 148 % and 54 % compared to the undoped hydrogels. The PPCI6-RE hydrogel demonstrating the best performance, was selected for cyclic loading-unloading tests. As illustrated in Fig. 2b, as strain increased from 100 % to 600 %, the area of the hysteresis loop grew but remained relatively low, with hysteresis under 1.5 J/m^3 and a dissipation coefficient around 0.1 at 600 % strain, indicating low tensile hysteresis (Fig. S11 in Supporting information). Ten cyclic loading-unloading tests conducted at strains of 100 %–400 % revealed consistently low hysteresis across all ranges, with only around 0.6 J/m^3 at 400 % strain and a dissipation coefficient of around 0.1 (Figs. 2c and d, Fig. S12 in Supporting information).

To explore its potential as a motion sensor, electrical tests were performed on the hydrogel. Rare-earth doping and crosslinking significantly enhanced sensitivity, and the strain detection range was notably extended due to the hydrogel's large deformation capacity. The PPCI6-RE hydrogel exhibited a gauge factor of 1.78 in the 0–350 % strain range and a gauge factor of 5.03 in the 350 %–1150 % range, demonstrating excellent strain sensitivity (Fig. 2e). Conductive tests on the PPCI6-RE hydrogel included a stepwise tensile-contraction test, which revealed consistent resistance signals at the same strain during both stretching and contraction phases, indi-

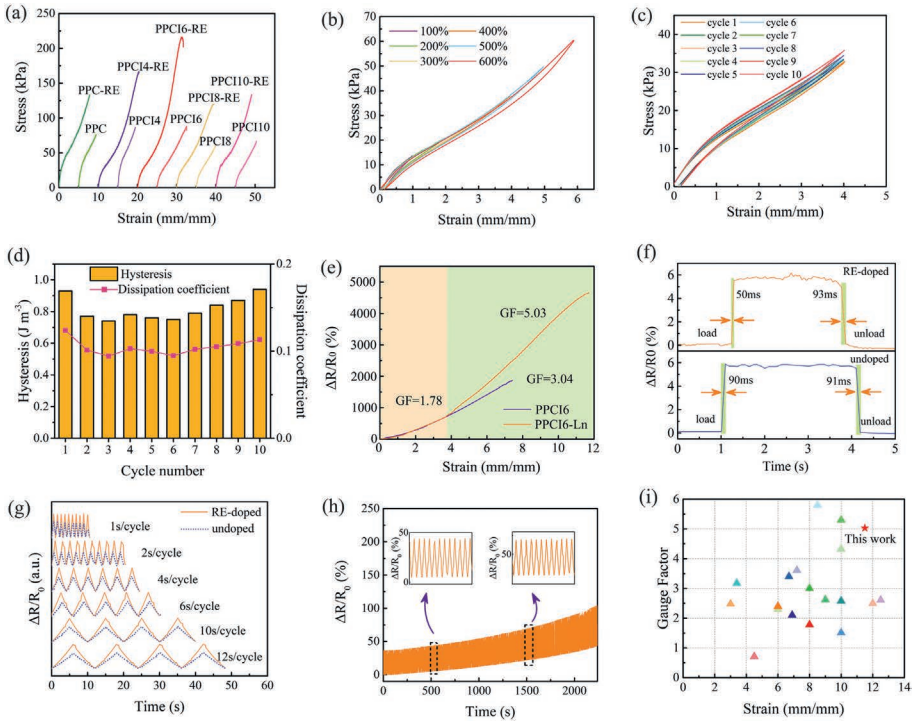


Fig. 2. Mechanical and sensing properties of hydrogels. (a) Tensile stress-strain curves of PPCI*x* and PPCI*x*-RE hydrogels. (b) Tensile loading-unloading cycles of PPCI6-RE at strains of 100%–600%. (c) 10 loading-unloading cycles of PPCI6-RE at 400% strain. (d) Hysteresis and dissipation coefficient over 10 cycles. (e) Gauge factor of PPCI6 and PPCI6-RE hydrogels. (f) Fast response and recovery times of PPCI6 (90/91 ms) and PPCI6-RE (50/93 ms) under light touch. (g) Resistance response of PPCI6 and PPCI6-RE at different frequencies under 100% strain. (h) Long-term cycle stability of PPCI6-RE over 700 cycles at 80% strain. (i) Comparison of tensile strain and gauge factor of existing conductive hydrogel sensors.

cating excellent strain-electrical signal response (Fig. S13a in Supporting information). Cyclic tensile tests at small strains (1%–9%) and larger strains (100%–400%) confirmed the hydrogel's sensing capabilities across a wide range (Figs. S13b and c in Supporting information). In small strain loading-unloading tests, the hydrogel displayed rapid loading and unloading responses of 50 and 93 ms, respectively (Fig. 2f). Subsequent tests at 100% strain across varying cycle speeds (1–12 s/cycle) revealed stable output signals at all speeds (Fig. 2g). In contrast, undoped hydrogels performed poorly, showing inconsistent signal-strain correspondence in stepwise tests, minimal resistance signal changes at different cycle speeds, unstable signals at large strains (300% and 400%), and longer response times during loading (90 ms). A cyclic test at 80% strain for 700 cycles demonstrated the hydrogel's excellent stability and repeatability (Fig. 2h). Moreover, to provide a visual representation of the trade-off between mechanical strain and sensitivity, we have included a strain-sensitivity (GF) scatter plot comparing our hydrogel with various reported hydrogels (Fig. 2i) [46–63]. The gauge factor of our hydrogel is comparable to or better than various reported conductive hydrogels with similar stretchability. Additionally, we compiled a table (Table S3 in Supporting information) summarizing the strain levels and cycle numbers tested in different studies, allowing for a direct comparison with our hydrogel, confirming that our hydrogel demonstrates good durability in cyclic deformation. These results provide strong evidence that our hydrogel is a promising candidate for flexible sensing applications.

Moreover, to elucidate the influence of rare-earth crosslinking on the deformation behavior, we compared the crazing and fracture morphologies of PPCI6 and PPCI6-RE hydrogels (Fig. S14 in Supporting information). Optical and SEM observations revealed that rare-earth doping delayed the onset of crazing from 240% to 355% strain and significantly reduced craze density and width. Moreover, unlike the vertical craze patterns seen in undoped samples, the doped hydrogels exhibited more complex deformation features, including fine lines parallel and oblique to the tensile direction. These findings indicate that rare-earth-induced crosslinking enhances the network's ability to redistribute stress and improves overall toughness by suppressing brittle fracture. Based on the experiments conducted, it is clear that crosslinking with rare-earth elements significantly affects the tensile properties of the hydrogel. According to rubber elasticity theory [63], the relationship between tensile modulus E (Pa) and the crosslink density v (mol/m^3) is defined as follows:

$$E = 3k_B T v / V_m \tag{1}$$

where k_B (J/K) is the Boltzmann constant, T (K) is the absolute temperature, and V_m is the molar volume. Additionally, the relationship between tensile stress σ (Pa) and strain ε (%) is given by:

$$\sigma = E/\varepsilon \tag{2}$$

Furthermore, the relationship between total energy density U (J/m^3) and strain is expressed as:

$$U = E\varepsilon^2/2 \tag{3}$$

From these equations, we can conclude that an excessive increase in crosslink density negatively impacts the stress-strain behavior of the hydrogels. Specifically, compared to the unmodified sample (PPC-RE), the introduction of a small amount of IDA (PPCI4-RE) increases the crosslink density, resulting in enhanced tensile stress and strain. As the IDA content rises further, an optimal balance is achieved, with the best mechanical properties observed in PPCI6-RE. However, excessive IDA content (PPCI8-RE and PPCI10-RE) results in overly rigid hydrogels, making them more susceptible to breaking.

In motion tests, the hydrogel's ability to adhere to various substrate surfaces is crucial for long-term stable signal monitoring. We selected PPCI6-RE for these experiments, and our findings indicate

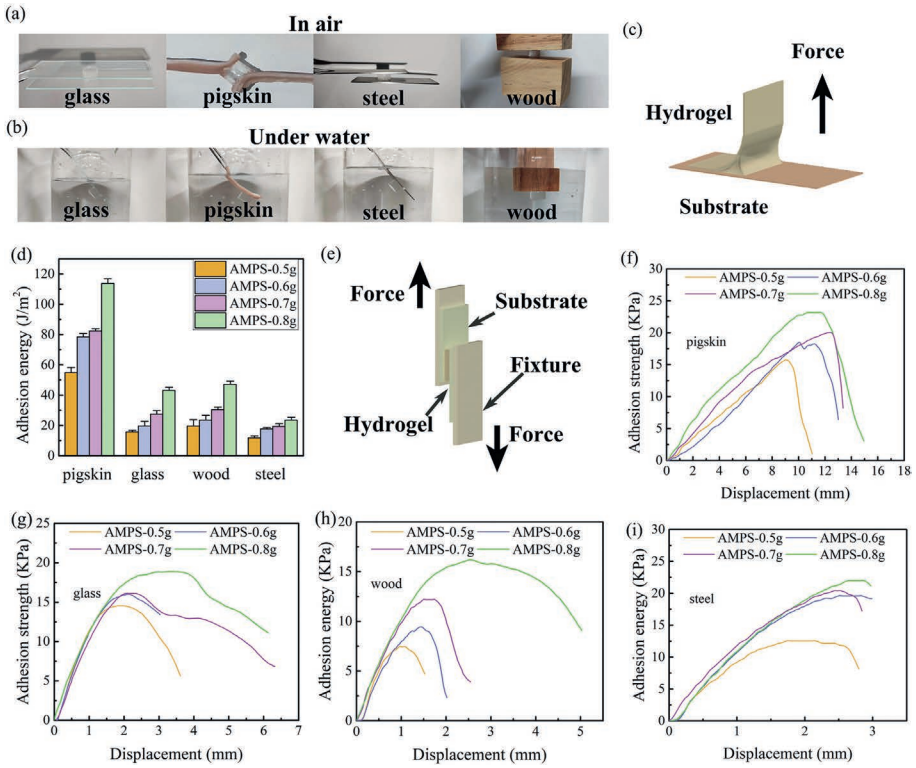


Fig. 3. (a, b) Adhesion of the hydrogel to various substrates in air and underwater. (c) Schematic of the peeling test. (d) Adhesion strengths of PPCI6-RE hydrogels to pigskin, glass, wood, and steel with varying AMPS concentrations. (e) Schematic of the lap shear test. (f–i) Lap shear adhesion curves of PPCI6-RE hydrogels on pigskin, glass, wood, and steel with different AMPS concentrations.

that the hydrogel can firmly adhere to glass, pigskin, steel plates, and wood, both in air and underwater (Figs. 3a and b).

We explored different AMPS contents, performing a 90° peeling test where the hydrogel was adhered to the substrate and then peeled off vertically (Fig. 3c). As the AMPS content increased, the adhesion energy of the hydrogel to various substrates improved. The highest hydrogel energy was observed with pigskin, reaching approximately 120 J/m^2, while the lowest was with steel at about 20 J/m^2, showing minimal variation with AMPS content (Fig. 3d). In tensile shear tests, the hydrogel with 0.8 g AMPS content demonstrated the highest instantaneous adhesion strength to pigskin, glass, wood, and steel, with values of 23, 19, 16, and 22 kPa, respectively (Figs. 3e-i). The hydrogel's strong adhesion to various substrates, particularly skin surfaces, primarily results from the -SO_3H groups in AMPS. These strongly polar group can form numerous hydrogen bonds and electrostatic interactions with hydroxyl (-OH), carboxyl (-COOH), and amino (-NH_2) groups on the skin surface [64–68]. In contrast, the more hydrophobic surfaces of steel, wood, and glass exhibit weaker chemical interactions with the hydrogel, making stable adhesion more challenging.

Given the hydrogel's high stretchability, recoverability, strain sensitivity, and excellent adhesion, it is well-suited for use as a wearable strain sensor. In this application, the hydrogel is adhered to the skin and connected at both ends to copper wires, which are interfaced with a Keithley 2400 digital source meter to record real-time electrical signals generated during various human activities. During movement, deformation of the hydrogel—either stretching or compression—leads to changes in its resistance, producing distinct and reproducible electrical signal patterns. The hydrogel can adhere firmly to the skin without external force, enabling stable monitoring of repetitive movements in finger joints, knees, wrists, and elbows (Figs. S15a-e in Supporting information). Additionally, it can track subtle skin movements such as speaking, blinking, and swallowing (Figs. S15f-h in Supporting information). Notably, when adhered to the surface of carotid artery, the hydrogel can accurately detect subtle strain signals like heartbeats, displaying distinct characteristic peaks of "P", "T", "N", and "D" (Fig. S15i in Supporting information).

Besides, we also studied the effect of adhesiveness on cyclic body movement. We found that the hydrogel containing 0.8 g of AMPS maintained stable signal output and strong adhesion over approximately 1000 consecutive cycles without detachment from the skin (Fig. S16 in Supporting information). In contrast, when the AMPS content was reduced to 0.7 g and 0.6 g, noticeable signal fluctuations appeared after around 300 and 150 cycles, respectively. Notably, at an AMPS content of 0.5 g, the hydrogel detached from the skin after only ~100 cycles, leading to a complete loss of sensing capability. These results clearly demonstrate that strong interfacial adhesion—enabled by sufficient AMPS content—is essential for maintaining long-term sensing stability under dynamic conditions.

In response to the growing demand for multi-channel optical/electrical sensors, we have developed an innovative weight detection sensor. This sensor consists of three layers: A bottom layer featuring a 3×3 UV LED array, a middle layer made up of a 3×3 array of rare-earth-doped hydrogels (with Tb doping at the vertices and center, and Eu doping at the midpoints of the edges), and a top pressing layer (Fig. 4a). The hydrogel transmits varying resistance signals based on changes in top pressure, activating the UV LEDs in different regions of the matrix to display red or green colors, thus indicating the magnitude of the pressure.

When the pressure is below the detection limit (*e.g.*, with an empty beaker), the hydrogel experiences minimal deformation, resulting in only slight change in resistance, and the UV LEDs remain off. Upon adding 15 mL water, when reaching the detection limit, the minimum pressure only ignite the middle hydrogel (Fig. 4b).

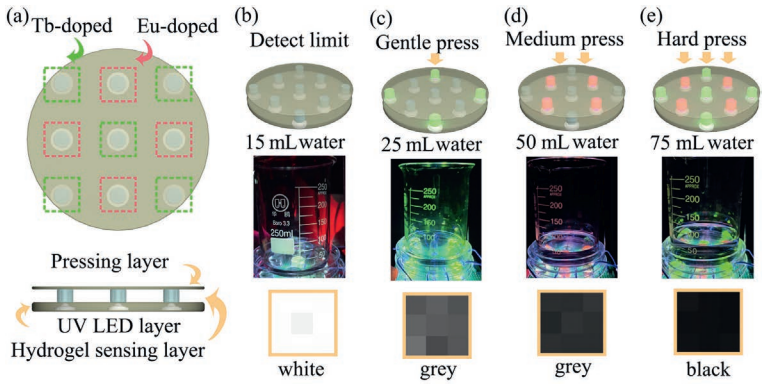


Fig. 4. The design strategy and application of fluorescent-conductive dual-channel sensor. (a) Structure of the sensor. Photographs of the sensor detecting different weights, showing detect limit (b) (15 mL water), (c) 25 mL water (green fluorescence), (d) 50 mL water (red fluorescence), and (e) 75 mL water (red and green fluorescence). At the bottom showing the visualization of pressure.

When adding 25 mL water, the lower pressure causes larger deformation in the hydrogel, leading to a significant resistance change that illuminates the Tb-doped hydrogel at the top corners, indicating green (Fig. 4c). With 50 mL water, moderate pressure induces further deformation, resulting in a larger resistance change that lights up the Eu-doped hydrogel at the midpoints of the edges, indicating red (Fig. 4d). When the water level exceeds 75 mL, greater pressure causes significant deformation, resulting in a significant resistance change that lights up all the hydrogels, producing a combination of red and green (Fig. 4e).

Additionally, we employed Processing software to enhance pressure visualization, transitioning from a white matrix (representing light pressure) to a black matrix (representing heavy pressure) (bottom of Figs. 4b-e). Our hydrogel matrix also allows for precise location pressure visualization. When specific areas of the hydrogel matrix are pressed (Figs. S17a-c in Supporting information) or when multiple points are pressed simultaneously (Figs. S17d and e in Supporting information), the corresponding hydrogels illuminate due to changes in the electrical signal, visually indicating the pressed areas. The pressure visualization in Processing is displayed as a 3×3 matrix of alternating black and white. Rare-earth ions (*e.g.*, Eu^{3+} and Tb^{3+}) offer ultra-narrow emission bands, high quantum yields, and excellent photochemical stability, outperforming conventional emitters like carbon dots that often suffer from broad spectra and signal interference [69,70]. By adjusting Eu/Tb ratios and IDA concentration, our hydrogel enables precise, modular tuning of fluorescence color and intensity across the visible range *via* controllable energy transfer. This system integrates dual-channel sensing into a simplified, structurally unified platform—combining luminescence and conductivity—allowing for scalable, real-time applications in wearable electronics.

This study successfully developed a novel multifunctional physically and chemically crosslinked rare-earth-doped hydrogel to address the limitations of traditional rare-earth fluorescent hydrogels in terms of conductivity, toughness, and adhesion. By introducing Eu^{3+} and Tb^{3+} ions to create stable physical crosslinking points with modified CMC-IDA, the hydrogel not only exhibits adjustable fluorescent properties but also significantly enhances its mechanical strength and conductivity. Additionally, this hydrogel demonstrates excellent high adhesion and low hysteresis, making it particularly suitable for sensing applications on skin surfaces. Furthermore, the rare-earth-doped hydrogel sensor with low detect limit enables precise pressure visualization through fluorescence color changes under varying pressures and can effectively monitor subtle human movements. This capability underscores its broad application potential in smart sensors and flexible electronics. In future work, we plan to develop highly sensitive and miniaturized hydrogel-based sensors to meet the requirements of wearable and human-interfacing applications. Our research provides new insights into the development of multifunctional rare-earth-doped hydrogels and is expected to make a significant impact in fields such as smart sensing.

CRediT authorship contribution statement

Kunda Yao: Writing – original draft, Software, Methodology, Investigation, Conceptualization. **Yue Shen:** Software, Methodology, Investigation. **Chao Chen:** Writing – review & editing, Software, Methodology. **Fengxiang Qin:** Validation, Project administration, Methodology. **Shuyan Song:** Project administration, Funding acquisition. **Xiaochen Dong:** Writing – review & editing, Supervision, Project administration. **Wei Liu:** Writing – review & editing, Project administration, Funding acquisition, Conceptualization.

Declaration of competing interest

The authors declare that they have no known competing financial interests or personal relationships that could have appeared to influence the work reported in this paper.

Acknowledgments

The authors acknowledge support from the Jilin Province Science and Technology Development Plan Funding Project (No. SKL202402014), National Natural Science Foundation of China (Nos. 22173047 and 22025506), and the Sino-German Mobility Program of the Sino-German Center for Research Promotion (No. M-0147). This research work was supported by the Open Funds of the State Key Laboratory of Rare Earth Resource Utilization (No. RERU2023003).

Supplementary materials

Supplementary material associated with this article can be found, in the online version, at doi:10.1016/j.cclet.2025.111531.

References

[1] G. Weng, S. Thanneeru, J. He, Adv. Mater. 30 (2018) 1706526.
[2] Z. Li, G. Wang, Y. Wang, et al., Angew. Chem. Int. Ed. 57 (2018) 2194–2198.
[3] S. Wei, W. Lu, X. Le, et al., Angew. Chem. Int. Ed. 58 (2019) 16243–16251.
[4] Q. Zhu, K. Van Vliet, N. Holten-Andersen, et al., Adv. Funct. Mater. 29 (2019) 1808191.
[5] X. Zhou, L. Wang, Z. Wei, et al., Adv. Funct. Mater. 29 (2019) 1903543.
[6] Y. Zhang, X. Le, Y. Jian, et al., Adv. Funct. Mater. 29 (2019) 1905514.
[7] K. Meng, C. Yao, Q. Ma, et al., Adv. Sci. 6 (2019) 1802112.
[8] H. Liu, S. Wei, H. Qiu, et al., Adv. Funct. Mater. 32 (2022) 2108830.

[9] X. Liu, B. Li, W. Wang, et al., Chem. Eng. J. 449 (2022) 137718.
[10] J.Y. Rodrigues Silva, L.L. da Luz, F.G. Martinez Mauricio, et al., ACS Appl. Mater. Interfaces 9 (2017) 16458–16465.
[11] Z. Zhang, Y. Li, L. Geng, et al., Inorg. Chem. 59 (2020) 3974–3982.
[12] R.J. Wang, W. Lu, Y. Zhang, et al., Chin. Chem. Lett. 34 (2023) 108086.
[13] G.Q. Yin, J.X. Huang, D.P. Liu, et al., Chin. Chem. Lett. 34 (2023) 107290.
[14] S. Wei, W. Lu, H. Shi, et al., Adv. Mater. 35 (2023) 2300615.
[15] R. Wang, Y. Zhang, W. Lu, et al., Angew. Chem. Int. Ed. 62 (2023) e202300417.
[16] H. Shi, S. Wu, M. Si, et al., Adv. Mater. 34 (2022) 2107452.
[17] Q. Wang, Z. Qi, Q.-M. Wang, et al., Adv. Funct. Mater. 32 (2022) 2208865.
[18] G. Lin, M. Si, L. Wang, et al., Adv. Opt. Mater. 10 (2022) 2102306.
[19] S. Wei, Z. Li, W. Lu, et al., Angew. Chem. Int. Ed. 60 (2021) 8608–8624.
[20] C. Chen, X. Pang, Y. Li, et al., Inorg. Chem. 62 (2023) 2105–2115.
[21] J. Li, W. Li, D. Xia, et al., Dyes Pigm. 166 (2019) 375–380.
[22] D.C. Jeong, J. Lee, Y. Lee, et al., Macromolecules 48 (2015) 1621–1626.
[23] M. Martinez-Calvo, O. Kotova, M.E. Moebius, et al., J. Am. Chem. Soc. 137 (2015) 1983–1992.
[24] J. Wang, S. Sun, B. Wu, et al., Macromolecules 52 (2019) 8643–8650.
[25] S. Alipour, A. Pourjavadi, S.H. Hosseini, Carbohydr. Polym. 310 (2023) 120610.
[26] Y. Chen, L. Li, J.Y. Zhang, et al., Chin. Chem. Lett. 35 (2024) 109102.
[27] X. Sun, Z. Qin, L. Ye, et al., Chem. Eng. J. 382 (2020) 122832.
[28] J. Fu, S.L. Zhang, L.R. Liang, et al., Chin. Chem. Lett. 35 (2024) 109804.
[29] B.H. Zhao, Z. Li, L. Zheng, et al., Chin. Chem. Lett. 35 (2024) 109810.
[30] X.M. Chen, Y.H. Feng, P. Zhang, et al., Adv. Mater. 37 (2025) 2413476.
[31] P. Zhang, Y.F. Yang, Z.B. Li, et al., Adv. Funct. Mater. 35 (2025) 2422869.
[32] J. Wang, T. Dai, H. Wu, et al., Compos. Sci. Technol. 221 (2022) 109345.
[33] Y. Gao, J. Chen, X. Han, et al., Adv. Funct. Mater. 30 (2020) 2003207.
[34] J. Tang, M. Wang, Y. Wang, et al., Sensor. Actuat. B: Chem. 403 (2024) 135174.
[35] C. Wang, Q. Han, P. Liu, et al., ACS Sensors 6 (2021) 252–258.
[36] C.W. Hwang, N.-S. Kwak, T.S. Hwang, Chem. Eng. J. 226 (2013) 79–86.
[37] B. Boulil, O. Henri-Rousseau, P. Blaise, Chem. Phys. 126 (1988) 263–290.
[38] N. Habibi, Spectrochim. Acta A 131 (2014) 55–58.
[39] M.S. Yeasmin, M.I.H. Mondal, Int. J. Biol. Macromol. 80 (2015) 725–731.
[40] W. Li, B. Sun, P. Wu, Carbohydr. Polym. 78 (2009) 454–461.
[41] M.R. Razak, N.A. Yusof, M.J. Haron, et al., Int. J. Biol. Macromol. 112 (2018) 754–760.
[42] L.T. Cuba-Chiem, L. Huynh, J. Ralston, et al., Langmuir 24 (2008) 8036–8044.
[43] Q. Ma, M. Zhang, C. Yao, et al., Chem. Eng. J. 394 (2020) 124894.
[44] Z.Y. Zhang, H. Zhu, Q.Q. Xu, et al., New J. Chem. 43 (2019) 13205–13211.
[45] T. Gorai, U. Maitra, Angew. Chem. Int. Ed. 56 (2017) 10730–10734.
[46] Z. Qin, X. Sun, Q. Yu, et al., ACS Appl. Mater. Interfaces 12 (2020) 4944–4953.
[47] X. Jing, X.Y. Wang, H.Y. Mi, et al., Mater. Lett. 237 (2019) 53–56.
[48] P. He, J. Wu, X. Pan, et al., J Mater. Chem. A 8 (2020) 3109–3118.
[49] C. Zheng, K. Lu, Y. Lu, et al., Carbohydr. Polym. 250 (2020) 116905.
[50] C. Cui, C. Shao, L. Meng, et al., ACS Appl. Mater. Interfaces 11 (2019) 39228–39237.
[51] Z. He, W. Yuan, Acs Appl. Mater. Interfaces 13 (2021) 1474–1485.
[52] H. Zhou, J. Lai, X. Jin, et al., Chem. Eng. J. 413 (2021) 127544.
[53] J. Chen, Q. Peng, T. Thundat, et al., Chem. Mater. 31 (2019) 4553–4563.
[54] G. Cai, J. Wang, K. Qian, et al., Adv. Sci. 4 (2017) 1600190.
[55] G. Ge, W. Yuan, W. Zhao, et al., J. Mater. Chem. A 7 (2019) 5949–5956.
[56] Y. Lu, X. Qu, S. Wang, et al., Nano Res. 15 (2022) 4421–4430.
[57] Q. Pang, H. Hu, H. Zhang, et al., ACS Appl. Mater. Interfaces 14 (2022) 26536–26547.
[58] M.I. Shekh, G. Zhu, W. Xiong, et al., Int. J. Biol. Macromol. 224 (2023) 604–620.
[59] Y. Luo, M. Yu, Y. Zhang, et al., Nano Energy 104 (2022) 107955.
[60] Y. Cheng, J. Zang, X. Zhao, et al., Carbohydr. Polym. 277 (2022) 118827.
[61] Y. Gao, Y. Gao, Z. Zhang, et al., J. Mater. Chem. C 10 (2022) 12873–12882.
[62] M. Wu, X. Wang, Y. Xia, et al., Nano Energy 95 (2022) 106967.
[63] P. Sotta, P.A. Albouy, M.Abou Taha, et al., Polymers 14 (2022) 9.
[64] Y. Xue, J. Zhang, X.M. Chen, et al., Adv. Funct. Mater. 31 (2021) 2106446.
[65] K. Zhang, X.M. Chen, Y. Xue, Adv. Funct. Mater. 32 (2021) 2111465.
[66] G. Chen, O. Hu, J. Lu, et al., Chem. Eng. J. 425 (2021) 131505.
[67] C. Cui, T. Wu, F. Gao, et al., Adv. Funct. Mater. 28 (2018) 1804925.
[68] L. Han, K. Liu, M. Wang, et al., Adv. Funct. Mater. 28 (2018) 1704195.
[69] B.Y. Wang, H.J. Cai, G. Waterhouse, et al., Small Sci. 2 (2022) 2200012.
[70] X. Miao, D. Qu, D.X. Yang, et al., Adv. Mater. 30 (2018) 1704740.